CrossMark

ORIGINAL ARTICLE

Phares L. Carroll · Guillaume Blanquart (iD)

A new framework for simulating forced homogeneous buoyant turbulent flows

Abstract This work proposes a new simulation methodology to study variable density turbulent buoyant flows. The mathematical framework, referred to as homogeneous buoyant turbulence, relies on a triply periodic domain and incorporates numerical forcing methods commonly used in simulation studies of homogeneous, isotropic flows. In order to separate the effects due to buoyancy from those due to large-scale gradients, the linear scalar forcing technique is used to maintain the scalar variance at a constant value. Two sources of kinetic energy production are considered in the momentum equation, namely shear via an isotropic forcing term and buoyancy via the gravity term. The simulation framework is designed such that the four dimensionless parameters of importance in buoyant mixing, namely the Reynolds, Richardson, Atwood, and Schmidt numbers, can be independently varied and controlled. The framework is used to interrogate fully non-buoyant, fully buoyant, and partially buoyant turbulent flows. The results show that the statistics of the scalar fields (mixture fraction and density) are not influenced by the energy production mechanism (shear vs. buoyancy). On the other hand, the velocity field exhibits anisotropy, namely a larger variance in the direction of gravity which is associated with a statistical dependence of the velocity component on the local fluid density.

Keywords Buoyant mixing · Variable density turbulence · Numerical forcing

1 Introduction

Turbulent buoyant flows are found in an array of naturally occurring processes (e.g., heat transfer within stars, supernovae formation, sub-sea hydrothermal vents), as well as in engineering applications (e.g., inertial confinement fusion, furnaces, accidental fires). The efficiency of these processes is dependent on the interplay between shear effects and buoyancy effects. The nature of this interplay is not entirely known, and simulation studies are commonly performed in an effort to advance the state of current understanding. Typically, simulation studies of turbulent buoyant mixing have focused on unstably stratified Rayleigh–Taylor (RT) flows (e.g., [1,2]). This configuration considers two fluids of differing densities that are unstably stratified in the presence of gravity. Density variations lead to differential fluid accelerations and fluid transfer from regions of high density to regions of low density. Traditionally, the pure fluid reservoirs are included in the simulation domain [1,2].

The use of unstable RT flows has enabled insightful examinations of variable density and turbulent buoyant mixing, and this geometry is commonly used to produce high-quality direct numerical simulation (DNS) data. For instance, from simulation studies of RT flows, it is known that buoyant flows differ from non-buoyant flows in the following ways. First, it was observed that buoyant flows have an asymmetric mixing rate. This manifests through a skewed density probability density function (PDF) and indicates that the more dense

---

P. L. Carroll · G. Blanquart (✉)
California Institute of Technology, 1200 East California Blvd., Pasadena, CA 91125, USA
E-mail: g.blanquart@caltech.edu

fluid in the RT unstable configuration mixes at a slower rate than the less dense fluid [3–5]. Second, as a consequence of this, the penetration depth of larger density fluids exceeds that of lower density fluids [3]. Third, distinct stages in the RT unstable mixing process have been identified, each with different governing dynamics [1]. Fourth, turbulent buoyant flows are known to be anisotropic as potential energy is converted into kinetic energy [6]. Lastly, while generally not a self-similar process, these flows may become self-similar under special circumstances [1,2,4]

However, this geometry is not ideal for parametric studies of buoyant flows. There are four main reasons for this. First, the inclusion of the pure fluid reservoirs can render sufficiently resolved simulations computationally expensive and, for all practical purposes (i.e., high Reynolds number), inaccessible. Second, the physics simulated are unsteady; throughout the process, the thickness of the mixing layer continues to increase. Third, the mixing process generated in a canonical RT geometry is subject to two sources of anisotropy: the (mean) density gradient (from global stratification) and the gravitational body force. This makes it difficult to ascribe the effects of each on the resultant mixing process. Lastly, the RT configuration couples the inertial effects and gravitational effects acting on the fluid system. A consequence of this is that Reynolds and Richardson numbers cannot be varied independently, limiting the utility of RT flows for parametric studies of turbulent buoyant mixing.

There are currently three simulation methods that offer alternatives to the classical RT unstable geometry for the study of buoyant mixing. The first alternative method was developed by Chung and Pullin [7]. This simulation method involves the use of a fringe region to continuously add high (low) density fluid at the top (bottom) of the simulation domain to maintain an unstably stratified RT flow. This perpetuates the variable density mixing process, enabling stationary statistics to be determined. It also mitigates the computational expense associated with including the pure fluid reservoirs in the domain. In summary, this fringe region-based approach addresses and resolves only two of the four nonidealities described above. Namely, the turbulent flow is still subject to two sources of anisotropy, preventing the attribution of specific aspects of the mixing problem to either gravity or globally acting (density) gradients, and gravitational and inertial effects remain linked.

The second alternative was developed first by Batchelor et al. [8] for the Boussinesq limit and then extended to variable density by Livescu et al. [3,4,6]. It is referred to as homogeneous Rayleigh–Taylor (HRT) or homogeneous buoyancy-generated turbulence. This approach does not include the pure reservoirs of fluids, but instead it makes use of a triply periodic, homogeneous box containing a variable density fluid. Gravity is applied to an initially quiescent velocity field, which drives the variable density fluid to a turbulent state. As the mixing process proceeds, the turbulent kinetic energy increases until a maximum is reached. After this, it decays due to the homogenization of the density field. Although this reduces the computational expense of the simulations, this approach remains unsteady, and mixing data can only be collected for a limited period of time. In addition, inertial and gravitational effects cannot be separated from one another.

The third framework, referred to as unstably stratified homogeneous (USH) turbulence, was developed recently by Soulard et al. [24]. It corresponds to a forced, buoyant simulation methodology analogous to the frequently used forced, homogeneous isotropic turbulence (HIT) simulation methods. HIT methods make use of source terms to create a state of statistically stationary turbulent mixing [9–12] and have enabled multiple parametric studies of turbulent mixing problems [13–17]. Analogous to HIT, the configuration of Soulard et al. [24] is triply periodic and is argued to be a small Atwood number Rayleigh–Taylor flow of an integral length scale much smaller than the mixing zone width. As for HRT, this framework allows for buoyant mixing to be less expensively interrogated than traditional RT flows, as the pure fluid reservoirs are not included in the simulated domain. In addition, the flows have the advantage of reaching a state of statistically stationary turbulence. Unfortunately, the framework remains nonideal: there are still two sources of anisotropy, namely gravity and the imposed mean scalar gradient, and gravitational and inertial effects cannot be varied independently.

Based on these observations, a simulation framework that combines all four critical requirements, namely reduced computational cost, statistically stationarity, no mean scalar gradient, and independence of inertial and gravitational effects, remains elusive. The objective of the present work is to develop such framework and to analyze the resulting turbulent buoyant flow field.

More precisely, the objective is to develop a statistically stationary version of HRT, yet without imposing anisotropy in the scalar field via an imposed scalar gradient as in USH. The ultimate goal is to quantify the contributions of all competing processes by varying *independently* four dimensionless groups, the Reynolds (Re), Richardson (Ri), Atwood (A), and Schmidt (Sc) numbers. The Reynolds number defines the relative strength of inertial and viscous forces, while the Richardson number defines the relative strength of gravitational and

inertial forces. The Schmidt number denotes the relative importance of kinematic viscosity to diffusivity, and the Atwood number indicates the extent of density variation present in the fluid system.

This paper is organized as follows. Section 2 describes the framework developed and the integration of numerical forcing methodologies. Global turbulent kinetic energy and scalar variance balances are also presented. Section 3 discusses the relevant four nondimensional parameters. Section 4 describes the results obtained from validation test cases. Lastly, Sect. 5 describes the means by which the nondimensional parameters can be adjusted to provide the desired turbulent buoyant flow conditions.

2 Proposed simulation methodology

The present analysis is focused on simple mixing, namely the mixing of two fluids with either different temperatures or different molecular weights. This type of mixing is often referred to as "two-fluid mixing," and multiple approaches have been used for the numerical simulations of such flows. The reader is referred to [18] for an extensive review. The present work relies on the low Mach number formulation of the Navier–Stokes equations [19,20], which has been used extensively for mixing (including stratified flows) and combustion applications [21–23]. The framework is first presented followed by a discussion of the velocity and scalar forcing techniques to be used.

2.1 Forced homogeneous buoyant turbulence

The computational domain in which the present framework is developed is that of a homogeneous, triply periodic box containing a variable density fluid. This is similar to the geometry adopted by Batchelor et al. [8], Livescu et al. [3,4,6], and Soulard et al. [24]. A box of turbulence is preferred as a geometry over the original RT configuration, as it reduces the computational cost of performing the simulations. The removal of any mean gradients (density or velocity) allows for periodicity and homogeneity to be assumed.

One could interpret this simulation domain as corresponding to a small volume inside of a buoyant mixing layer (not necessarily a Rayleigh–Taylor mixing layer) after the mixing process has begun, but before fluid mixing has ended [24]. It could also be seen as the state of peak turbulent kinetic energy found in HRT, when energy production by buoyancy forces balances (temporarily) energy dissipation by viscous forces [6,8]. In an attempt to differentiate it from the unsteady HRT configuration, the present framework will be referred to as forced homogeneous buoyant turbulence or HBT.

2.2 Governing equations

In the low Mach formulation [19], the governing equations needed to describe variable density mixing are the continuity equation (Eq. 1), the momentum equation (Eq. 2), and the scalar transport equation (Eq. 3),

$$\frac{\partial \rho}{\partial t} + \frac{\partial \rho u_j}{\partial x_j} = 0, \tag{1}$$

$$\frac{\partial \rho u_i}{\partial t} + \frac{\partial \rho u_i u_j}{\partial x_j} = -\frac{\partial p}{\partial x_i} + \frac{\partial \tau_{ij}}{\partial x_j} + (\rho - \langle \rho \rangle) g_i + f_{u_i}, \tag{2}$$

$$\frac{\partial \rho Z}{\partial t} + \frac{\partial \rho Z u_j}{\partial x_j} = \frac{\partial}{\partial x_j} \left(\rho \mathcal{D} \frac{\partial Z}{\partial x_j} \right) + f_Z. \tag{3}$$

Throughout this paper, ρ represents the density, $\langle \rho \rangle$ represents the ensemble average density, u_i represents the i-component of velocity, $\mathcal{D}$ is the molecular diffusivity, ν is the kinematic viscosity, $\mu = \nu \rho$ is the dynamic viscosity, and $\tau_{ij} = \mu \left(\frac{\partial u_i}{\partial x_j} + \frac{\partial u_j}{\partial x_i} \right) - \frac{2}{3} \mu \frac{\partial u_k}{\partial x_k} \delta_{ij}$ is the deviatoric contribution to the stress tensor. Here, ν and $\mathcal{D}$ are spatially constant, making the Schmidt number ($Sc = \nu / \mathcal{D}$) spatially constant; any changes in density correspond to an equivalent change in the dynamic viscosity and diffusivity.

Consistently with previous studies [23], the hydrodynamic pressure is decomposed as the sum of the hydrostatic pressure head, $\langle \rho \rangle g_i x_i$, and fluctuations around this hydrostatic pressure, p. As evidenced by this decomposition, the ensemble average of the pressure fluctuations is zero, $\langle p \rangle = 0$. This decomposition has the advantage of rendering the system of equations homogeneous (and periodic), even in the presence of gravity.

The scalar quantity, Z, is related to the local composition of the mixture and can be thought of as either a nondimensional temperature or the local mass fraction of one of the two fluids being mixed. The exact definition of this scalar quantity and its relationship to the mixture density are discussed in more detail in the following section.

As in USH turbulence [24], the role of the scalar source term, f_Z, is to sustain the scalar field at a constant variance. This prevents the scalar field from homogenizing. In turn, a heterogeneous scalar field ensures, via the equation of state (Eq. 5), a heterogeneous density field. With a nonhomogeneous density field, the effects of both buoyant (body) forces and pseudo-shear forces can be investigated. On the one hand, the influence of the buoyant body force, $(\rho - \langle \rho \rangle) g_i$, is determined by the magnitude of the gravity vector, g_i. On the other hand, the influence of the pseudo-shear term is determined by the magnitude of the isotropic source term, f_{u_i}. When mixing is driven by shear ($g_i = 0$), HIT is recovered; when mixing is driven by gravity ($f_{u_i} = 0$), HBT is recovered.

2.3 Equation of state

The main difference between the fully compressible Navier–Stokes equations and the low Mach number formulation is in the equation of state. In the low Mach number formulation, the hydrodynamic pressure (present in Eq. 2) does not appear in the equation of state; only the background/thermodynamic pressure does [19]. In other words, the mixture density is entirely determined by the local temperature and mixture molecular weight (assuming an ideal gas).

As mentioned earlier, we focus on "two-fluid mixing," i.e., the mixing between two fluids with either different molecular weights or different temperatures. For the first case, fluid 1 (resp. 2) has a mass fraction Y_1 (resp. $Y_2 = 1 - Y_1$) and a molecular weight W_1 (resp. W_2). The mixture density is given by

$$\rho = \frac{P_0}{RT} \left[\frac{Y_1}{W_1} + \frac{1 - Y_1}{W_2} \right]^{-1}, \tag{4}$$

with R the universal gas constant, T the temperature (constant during mixing), and P_0 the thermodynamic pressure. The scalar Z is often defined as the mass fraction of one of the two fluids (i.e., $Z = Y_1$), and hence, it is physically bounded, $0 \leq Z \leq 1$. For reasons that will become more apparent in the following section (and without loss of generality), it is more convenient to define Z as the deviations away from the state where the two fluids are perfectly mixed. For instance, for a domain composed equally of fluid 1 and 2, the new scalar Z would be defined as $Z = Y_1 - 0.5$. With this simple shift, the scalar Z has a distribution about a zero mean.

After re-arrangement of Eq. 4, the mixture density takes the form

$$\rho = \frac{1}{aZ + b}, \tag{5}$$

where a and b are constants that determine the variance and the mean of the density field, respectively. They are more fully detailed in Sect. 4.2. Considering mixing of two fluids with different temperatures would lead to the same final equation (Eq. 5). This equation defines the density at every point in the domain based on the fluctuating scalar value at that point. It is important to note that within the present low Mach number formulation, there is no limit on the range of density fluctuations or equivalently Atwood numbers to be investigated (see Sect. 4.3).

2.4 Necessary restrictions on forcing methods

Without assuming a specific velocity or scalar field forcing method, four conditions are required to implement the proposed approach. These constraints are obtained by considering the implications of statistical stationarity.

Following a Reynolds decomposition, all variables are decomposed into the sum of an ensemble average, $\langle \cdot \rangle$, and a fluctuating component, $(\cdot)'$, according to: $\rho = \langle \rho \rangle + \rho'$, $u_i = \langle u_i \rangle + u_i'$, and $Z = \langle Z \rangle + Z'$. Statistical stationarity implies,

$$\frac{\partial \langle \rho \rangle}{\partial t} = 0, \quad \frac{\partial \langle \rho u_i \rangle}{\partial t} = 0, \quad \frac{\partial \langle \rho Z \rangle}{\partial t} = 0. \tag{6}$$

Physically, these correspond to a constancy in density, momentum, and scalar concentration. For the current purposes, and without loss of generality, the average values of momentum and scalar concentration are chosen to be zero,

$$\langle \rho u_i \rangle = 0, \tag{7}$$

$$\langle \rho Z \rangle = \langle \rho Z \rangle_{t=0} = 0. \tag{8}$$

Returning to the forced momentum and forced scalar transport equations (Eqs. 2 and 3), when ensemble-averaged, they reduce to,

$$\frac{\partial \langle \rho u_i \rangle}{\partial t} = \langle f_{u_i} \rangle = 0, \tag{9}$$

$$\frac{\partial \langle \rho Z \rangle}{\partial t} = \langle f_Z \rangle = 0. \tag{10}$$

Here, the condition of homogeneity has been applied, under which spatial derivatives of ensemble-averaged terms vanish. It is important to remember that homogeneity (invariance by translation) does not imply isotropy (invariance by rotation). The present turbulent buoyant flows are homogeneous, but not isotropic because of the presence of gravity.

Equations 7–10 constitute the four needed constraints for the system of forced governing equations. To this point, the presented equations have been general; no specific forcing method for either the velocity field or scalar field has been offered. Specific forms for the two source terms are now provided.

2.5 Velocity field forcing

In variable density flows, fluid mixing is driven primarily by two mechanisms, shear and buoyancy. The forcing term, f_{u_i}, and the body force term, $\rho' g_i$, in Eq. 2 are meant to model these two processes. The effects of shear are modeled by f_{u_i}, which necessitates that the implemented velocity field forcing source term be chosen with care. The velocity field forcing method [25] used in this study is a modification of Lundgren's linear velocity forcing scheme [10,11]. This is motivated by its analogy to a shear term, the physical mechanism responsible for the development of turbulence in real flows. Further, Lundgren's linear forcing method has been shown to be more consistent with turbulent statistics reported in decaying wind tunnel experiments than those generated using low waveband spectral forcing approaches [27,28]. Additionally, Lundgren's method is more easily adaptable to variable density flow conditions.

By including a non-buoyant source term in the governing momentum equation, pseudo-shear effects can be considered together with and separate from buoyant effects. The momentum source term for the linear forcing approach takes the form,

$$f_{u_i} = \frac{Q}{k} \rho u_i, \tag{11}$$

where Q is a constant forcing coefficient related to the energy dissipation rate, ϵ, which is defined as,

$$\epsilon = \frac{1}{\langle \rho \rangle} \langle 2\mu S_{ij} S_{ij} \rangle = \frac{1}{\langle \rho \rangle} \left\langle \frac{\mu}{2} \left(\frac{\partial u_i}{\partial x_j} + \frac{\partial u_j}{\partial x_i} \right)^2 \right\rangle, \tag{12}$$

and k is the instantaneous turbulent kinetic energy, which is defined as,

$$k = \frac{1}{\langle \rho \rangle} \left\langle \frac{1}{2} \rho u_i u_i \right\rangle. \tag{13}$$

Equation 11 is a pseudo-shear term [10]. The coefficient Q determines the amplitude of the forcing, and, in purely isotropic turbulent flows ($g_i = 0$), it imposes an energy dissipation rate on the simulated turbulence. Since the forcing term acts only on the fluctuations in fluid momentum, ρu_i, it imparts, on average, the same magnitude of momentum flux in the three ordinate directions, making it an isotropic source term. With the above momentum source term, Eq. 9 is verified due to Eq. 7, and the forced momentum equations become,

$$\frac{\partial \rho u_i}{\partial t} + \frac{\partial \rho u_i u_j}{\partial x_j} = -\frac{\partial p}{\partial x_i} + \frac{\partial \tau_{ij}}{\partial x_j} + \frac{Q}{k} \rho u_i + \rho' g_i. \tag{14}$$

The turbulent kinetic energy equation can be obtained by multiplying Eq. 14 by u_i. After manipulation and using mass conservation (Eq. 1), it is found,

$$\frac{\partial \frac{1}{2}\rho u_i^2}{\partial t} + \frac{\partial \frac{1}{2}\rho u_i^2 u_j}{\partial x_j} = -\frac{\partial p u_i}{\partial x_i} + p\frac{\partial u_i}{\partial x_i} + \frac{\partial \tau_{ij} u_i}{\partial x_j} - \tau_{ij}\frac{\partial u_i}{\partial x_j} + \frac{Q}{k}\rho u_i^2 + \rho' g_i u_i. \tag{15}$$

After ensemble averaging, using the definitions of kinetic energy, k, and dissipation, ϵ, using that $\langle\rho\rangle$ is constant, and applying homogeneity ($\nabla \cdot \langle\rangle = 0$), the energy equation reduces to,

$$\frac{\partial k}{\partial t} = \frac{1}{\langle\rho\rangle}\left(\left\langle p\frac{\partial u_i}{\partial x_i}\right\rangle + \frac{2}{3}\left\langle \mu\left(\frac{\partial u_i}{\partial x_i}\right)^2\right\rangle\right) - \epsilon + 2Q + \frac{1}{\langle\rho\rangle}\langle\rho' u_i\rangle g_i. \tag{16}$$

This expression states that the time rate of change of kinetic energy is a balance between two dilatation terms, energy dissipation and energy production from isotropic and anisotropic (buoyant) sources. A steady state manifests when dissipation grows sufficiently to counter the other contributing terms. At steady state, it can be written,

$$\epsilon = \frac{1}{\langle\rho\rangle}\left(\left\langle p\frac{\partial u_i}{\partial x_i}\right\rangle + \frac{2}{3}\left\langle \mu\left(\frac{\partial u_i}{\partial x_i}\right)^2\right\rangle\right) + 2Q + \frac{1}{\langle\rho\rangle}\langle\rho' g_i u_i\rangle. \tag{17}$$

The two dilatation terms are present regardless of the source of turbulence (buoyancy or pseudo-shear) and are found in all numerical tests (Sect. 4) to account for no more than 2 % of the stationary energy dissipation rate (ϵ).

From Eq. 17, a power density ratio, denoted by α, can be expressed,

$$\alpha = \frac{P_{\text{buoy}}}{P_{\text{buoy}} + P_{\text{shear}}} = \frac{\langle\rho' g u_i\rangle\delta_{i,2}}{\langle\rho' g u_i\rangle\delta_{i,2} + 2Q\langle\rho\rangle}. \tag{18}$$

The power density ratio so defined is an indicator of the amount of power injected into the mixing fluids from purely buoyant forces relative to the total power being injected into the fluids. A value of $\alpha = 0$ indicates a purely non-buoyant mixing process, while a value $\alpha = 1$ indicates a purely buoyant mixing process. Thus, by adjusting the values of Q and g, the proposed equations can model all flows from fully isotropic, pseudo-shear ($g = 0$, $\alpha = 0$) to purely buoyant ($Q = 0$, $\alpha = 1$) turbulent conditions.

2.6 Scalar field forcing

In buoyant flows, there are two sources of anisotropy in the velocity field. These sources are gravity and the scalar being advected. If the scalar field is anisotropic, this can couple back on the flow dynamics via the density field (Eq. 5), promoting the permeation of anisotropy into the velocity field. The most commonly used scalar forcing method applies a mean spatial gradient across the scalar field as a means of generating a statistically stationary scalar field [14,15]. Previous studies of unstably stratified homogeneous (USH) turbulence have relied on such mean scalar gradient (in the direction of gravity) to prevent complete homogenization of the scalar field [24]. Unfortunately, with such forcing technique, it is unclear whether the subsequent anisotropic nature of the velocity field is due to the scalar forcing technique or the presence of gravity.

In this work, the source of anisotropy in the scalar field is eliminated by adopting a scalar field forcing method that has no preferred direction or directional dependence. This forcing method, termed the linear scalar forcing method [26], does not assume any particular scalar field distribution, nor does it enforce one. It simply preserves the (isotropic or non-isotropic) character of the scalar field. Consequently, this provides a means by which to isolate the impact that buoyancy alone has on turbulent mixing. The linear scalar forcing term takes the form,

$$f_Z = \left(\frac{1}{\tau_I}\left(\frac{\beta}{\sigma_Z} - 1\right) + \frac{\chi}{2\sigma_Z^2}\right)\rho Z, \tag{19}$$

where τ_I is an inertial timescale, β^2 is the long-time steady-state variance to which the scalar field is compelled to evolve, and σ_Z^2 and χ are the instantaneous scalar field variance and scalar dissipation rate, respectively. These are defined as,

$$\sigma_Z^2 = \frac{1}{\langle\rho\rangle}\langle\rho Z^2\rangle,$$ (20)

$$\chi = \frac{1}{\langle\rho\rangle}\left\langle 2\rho\mathcal{D}\frac{\partial Z}{\partial x_j}\frac{\partial Z}{\partial x_j}\right\rangle.$$ (21)

It follows that the final advection–diffusion equation can be written,

$$\frac{\partial\rho Z}{\partial t} + \frac{\partial\rho Z u_j}{\partial x_j} = \frac{\partial}{\partial x_j}\left(\rho\mathcal{D}\frac{\partial Z}{\partial x_j}\right) + \left(\frac{1}{\tau_I}\left(\frac{\beta}{\sigma_Z} - 1\right) + \frac{\chi}{2\sigma_Z^2}\right)\rho Z.$$ (22)

When Eq. 22 is multiplied by the fluctuating scalar quantity, Z, and ensemble-averaged, an evolution equation for the scalar field variance emerges,

$$\frac{\partial\sigma_Z^2}{\partial t} = 2\frac{\sigma_Z^2}{\tau_I}\left(\frac{\beta}{\sigma_Z} - 1\right).$$ (23)

The linear scalar forcing drives the scalar field to a specified variance value. When the standard deviation of the scalar field reaches this value ($\sigma_Z = \beta$), the right-hand side of Eq. 23 vanishes. This induces a statistically stationary state in the scalar field and, hence, in the density field through Eq. 5.

3 Relevant nondimensional parameters

3.1 Definitions

As mentioned earlier, the four dimensionless groups of primary importance in turbulent buoyant flows are the Atwood, Schmidt, Reynolds, and Richardson numbers.

The Atwood number, A, indicates the extent of density variation in the mixing fluids. It is defined traditionally as,

$$A = \frac{\rho_2 - \rho_1}{\rho_2 + \rho_1},$$ (24)

where ρ_1 and ρ_2 are the densities of the two fluids being mixed. The larger the difference in the densities of the pure fluids, the larger the Atwood number. In the present work, an alternative definition of the Atwood number is used,

$$A = \frac{\sigma_\rho}{\langle\rho\rangle},$$ (25)

where σ_ρ is the standard deviation of the density field and $\langle\rho\rangle$ is the mean density. The standard deviation of the density is informative of the spread in density values throughout the domain, as there are not any regions of pure fluids at ρ_1 or ρ_2.

The scalar field evolution is controlled by the Schmidt number,

$$Sc = \frac{\nu}{\mathcal{D}},$$ (26)

which is indicative of the relative strength of viscous (fluid) diffusion versus molecular (scalar) diffusion (e.g., thermal conductivity).

To express the Reynolds and Richardson numbers, it is necessary to define characteristic length scales and velocity scales. The current work adopts the following definitions. For the velocity scale, the root-mean-square of the velocity field is taken, and it is calculated according to,

$$u_{\text{RMS}} = \sqrt{\frac{1}{3}\left(\frac{\langle\rho u^2\rangle}{\langle\rho\rangle} + \frac{\langle\rho v^2\rangle}{\langle\rho\rangle} + \frac{\langle\rho w^2\rangle}{\langle\rho\rangle}\right)}.$$ (27)

The characteristic length scale, in turn, is defined as,

$$l = \frac{u_{\text{RMS}}^3}{\epsilon}. \tag{28}$$

Following Eqs. 27 and 28, the Reynolds number is defined as,

$$Re = \frac{u_{\text{RMS}}\, l}{\nu}, \tag{29}$$

and the Richardson number is defined as,

$$Ri = \frac{Agl}{u_{\text{RMS}}^2}. \tag{30}$$

3.2 Nondimensional governing equations

The roles played by inertia, gravity, density variation, and other physical properties in the mixing process can be understood by nondimensionalizing the continuity (Eq. 1), momentum (Eq. 14), and scalar transport (Eq. 22) equations. Using characteristic length, time, and velocity scales, pertinent flow variables can be nondimensionalized as,

$$\hat{\rho} = \frac{\rho}{\langle\rho\rangle}, \quad \hat{u}_i = \frac{u_i}{u_{\text{RMS}}}, \quad \hat{p} = \frac{p}{\langle\rho\rangle\, u_{\text{RMS}}^2}, \quad \hat{x}_i = \frac{x_i}{l}, \quad \hat{t} = \frac{t}{\tau_c}, \quad \hat{Z} = \frac{Z}{\sigma_Z},$$

where $(\hat{\cdot})$ variables are unitless and of order one, and $\tau_c = l/u_{\text{RMS}}$.

Variable density flows can be classified as either Boussinesq or non-Boussinesq types, and the nondimensional form of the continuity equation can be used to illustrate the distinction. Using the defined characteristic scales, the continuity equation can be written,

$$A\frac{D\rho'/\sigma_\rho}{D\hat{t}} + \hat{\rho}\frac{\partial\hat{u}_j}{\partial\hat{x}_j} = 0. \tag{31}$$

As the density fluctuations scale with the standard deviation of the density field, the ratio ρ'/σ_ρ is of order one. The derivatives of the mean density vanished due to homogeneity and stationarity. A Boussinesq flow has only a weak variation in density, and the Atwood number approaches zero. This reduces the material derivative to zero, the incompressible limit is recovered, and the velocity field becomes divergence free. As a result, the density is assumed constant everywhere except in the gravitational term [29]. Under non-Boussinesq conditions, the Atwood number is nonzero, and the velocity field retains a nonzero divergence.

The momentum equation can be examined similarly. When the (forced) momentum equation is nondimensionalized, it is obtained,

$$\frac{\partial\hat{\rho}\hat{u}_i}{\partial\hat{t}} + \frac{\partial\hat{\rho}\hat{u}_i\hat{u}_j}{\partial\hat{x}_j} = -\frac{\partial\hat{p}}{\partial\hat{x}_i} + \frac{1}{Re}\frac{\partial}{\partial\hat{x}_j}\left\{\hat{\rho}\left(\frac{\partial\hat{u}_i}{\partial\hat{x}_j} + \frac{\partial\hat{u}_j}{\partial\hat{x}_i}\right) - \frac{2}{3}\hat{\rho}\frac{\partial\hat{u}_k}{\partial\hat{x}_k}\delta_{ij}\right\}$$
$$+ \tau_c\frac{Q}{k}\hat{\rho}\hat{u}_i + Ri\,\frac{\rho'}{\sigma_\rho}\delta_{i,2}. \tag{32}$$

Note that the non-buoyant forcing term contains a ratio of timescales. The forcing amplitude, Q, has units of an energy dissipation rate, such that its ratio with the turbulent kinetic energy, k, yields a timescale related to the eddy turnover timescale. The left-hand side of Eq. 32 is of order one, and the right-hand side clarifies the effect of varying Re or Ri. If Re is increased, the viscous term is reduced in magnitude, and the inertial terms become increasingly dominant. If Ri is increased, the magnitude of the buoyant term grows relative to inertia.

Lastly, the (forced) advection–diffusion equation is addressed. Here, the forcing term is written in terms of a scalar timescale ($\tau_Z = \sigma_Z^2/\chi$) and $\beta = \sigma_Z$ is assumed. The nondimensional form of the advection–diffusion equation is,

$$\frac{\partial\hat{\rho}\hat{Z}}{\partial\hat{t}} + \frac{\partial\hat{\rho}\hat{u}_j\hat{Z}}{\partial\hat{x}_j} = \frac{1}{ReSc}\frac{\partial}{\partial\hat{x}_j}\left(\hat{\rho}\frac{\partial\hat{Z}}{\partial\hat{x}_j}\right) + \frac{\tau_c}{2\tau_Z}\hat{\rho}\hat{Z}. \tag{33}$$

From this expression, increasing either the *Re* or *Sc* numbers reduces the relative importance of scalar diffusion; conversely, decreasing either parameter increases the importance of scalar diffusion. The product of the *Re* and *Sc* numbers is also referred to as the Peclet number. As with the momentum equation, the effect of the scalar forcing term is to impose a timescale.

4 Simulation framework validation

4.1 Code description

The simulation code used in this work is NGA [21], which is an extension of the high order conservative finite difference scheme developed by Morinishi et al. [30]. It is discretely conservative of mass, momentum, and kinetic energy, and it can provide an arbitrarily high order of accuracy. NGA makes use of staggered variables (in time and space) [31] to ensure high accuracy with a compact stencil when evaluating derivatives.

NGA solves the mass conservation (Eq. 1), momentum conservation (Eq. 2), and scalar transport (Eq. 3) equations. The system of equations is closed by connecting the scalar field to the density field via an equation of state (Eq. 5). The NGA code makes use of a fractional step approach based on a predictor–corrector formulation [32,33]. Only a brief overview of the fractional step procedure is given below. More details can be found in [33,34]. An iterative procedure (where the subscript k denotes the iteration number) is used to advance the momentum equations from a time step n to the new time step $n + 1$ and the scalar equations from a time step $n + 1/2$ to the new time step $n + 3/2$.

1. Solve the mixture fraction equation (Eq. 3) for $Z_{k+1}^{n+3/2}$ using the velocity u_k^{n+1}.
2. Evaluate the density, $\rho_{k+1}^{n+3/2}$, using the equation of state (Eq. 5).
3. Predict the momentum by solving the momentum equation (Eq. 2) for ρu_{k+1}^*.
4. Solve a (fixed coefficient) Poisson system for the pressure correction, δp_{k+1}

$$\nabla^2 \left(\delta p_{k+1} \right) = \frac{1}{\Delta t} \left[\frac{\rho_{k+1}^{n+3/2} - \rho^{n+1/2}}{\Delta t} + \nabla \cdot \rho u_{k+1}^* \right] \tag{34}$$

5. Correct the momentum to ensure continuity (Eq. 1) is satisfied discretely and update the pressure field

$$\rho u_{k+1}^{n+1} = \rho u_{k+1}^* - \Delta t \nabla \delta p_{k+1} \tag{35}$$

$$p_{k+1}^{n+1} = p_k^{n+1} + \delta p_{k+1} \tag{36}$$

6. Iterate back to step 1 until sufficient convergence (in practice, four sub-iterations were found sufficient).

For the current work, the momentum equation is solved using second-order spatial accuracy in both the convective and viscous terms. It was found that increasing to higher orders had negligible impact on the data obtained. For the scalar field, a minimally dissipative, fifth-order HOUC scheme was implemented [35]. The procedure to solve this system of equations includes a second-order semi-implicit Crank–Nicolson time-advancement scheme for the velocity and scalars [21,33].

In all simulation data to be presented, the meshes are strictly uniform. As mentioned earlier, the boundary conditions for all equations are triply periodic. The velocity, scalar, and density fields are initialized following Eswaran and Pope [12,13]. In the present case, the initial pressure is set to zero for simplicity. Recall that the pressure is not the full hydrodynamic pressure, but only the fluctuations around the hydrostatic pressure head (see Sect. 2.2).

4.2 Numerical tests

To investigate how the physics of mixing changes under buoyant and non-buoyant (pseudo-shear) conditions, a parametric simulation study spanning a broad range of conditions using the proposed forced approach is conducted. There are three classes of simulations performed. Note that, in all simulations, the Atwood and Schmidt numbers are held fixed; this is done to facilitate comparisons. Also, the width of the domain is set to 2π in all cases.

Table 1 (Pseudo) shear-driven turbulent flows under the proposed configuration with $Sc = 1$, $A = 0.13$, and $\alpha = 0$

No.	ϵ	Q	Re	$|g|$	Ri	$\kappa_{max}\eta$	N^3
Se01	0.12	0.065	122	0	0	1.55	96^3
Se05	0.53	0.301	217	0	0	1.41	128^3
Se1	0.96	0.519	248	0	0	1.83	192^3
Se2	2.01	1.07	326	0	0	2.02	256^3
Se4	3.88	2.00	405	0	0	2.57	384^3
Se6	5.80	3.03	515	0	0	2.33	384^3
Ie2	2.01	1.07	417	0	0	2.02	256^3

Note that case Ie2 corresponds to a (incompressible) constant density simulation. Ia0e2 is included for comparison purposes in Sect. 5

Table 2 Buoyantly driven turbulent flows under the proposed configuration with $Sc = 1$, $A = 0.13$, and $\alpha = 1$

No.	ϵ	Q	Re	$|g|$	Ri	$\kappa_{max}\eta$	N^3
Be005	0.05	0	193	1	1.10	1.96	96^3
Be008	0.08	0	231	1.50	1.10	1.74	96^3
Be009	0.09	0	265	1.75	1.10	1.64	96^3
Be010	0.10	0	231	2	1.10	1.60	96^3
Be05	0.50	0	541	5	1.10	1.44	128^3
Be1	1.02	0	654	8	1.10	1.81	192^3
Be2	2.22	0	957	12	1.10	1.99	256^3
Be4	4.02	0	934	18	1.10	2.57	384^3
Be5	5.27	0	1240	20	1.10	2.40	384^3

The first class of simulations corresponds to purely non-buoyant conditions, similar to homogeneous isotropic turbulence (HIT) simulations of variable density mixing. These cases are listed in Table 1, and they are characterized by a power density ratio of $\alpha = 0$. These non-buoyant cases span a sufficient range of energy dissipation rates, which is here used as a proxy for the Reynolds number, such that meaningful inferences about the impact of the simulation framework on the generated flow fields can be determined. The test cases are denoted in Table 1 by their mixing mechanism (shear, "S") and their stationary energy dissipation rate (ϵ, "e"). One incompressible, constant density simulation is included, and it is denoted by "I" followed by its dissipation rate "e."

The second class of simulations uses only buoyant forcing. In these cases, the linear velocity forcing is set to zero ($Q = 0$), and the only source of power for the fluid system comes from the gravitational body force. Accordingly, these buoyant simulations have a power density ratio of $\alpha = 1$, and they are delineated in Table 2. As with the non-buoyant data, a substantial range of energy dissipation rates are covered so that the effects of the simulation framework on the resultant flow fields could be determined. The test cases are denoted in Table 2 by their mixing mechanism (buoyancy, "B") and their stationary energy dissipation rate (ϵ, "e").

The final class of simulations included in this work corresponds to cases with both non-buoyant (pseudo-shear) effects and buoyant effects, and these have power density ratios bounded by $0 < \alpha < 1$. These partially buoyant simulations are listed in Table 3. More test cases are performed for this class of flows, as there is a greater span of α space to explore. The test cases are denoted in Table 3 by their mixing mechanism (partial buoyancy and partial shear, "P"), their power density ratio (α, "a"), and their stationary energy dissipation rate (ϵ, "e").

While all test cases are presented in the current work, for illustrative purposes, four test cases are presented in greater detail than the rest (Table 4). These four cases are taken as representative, and their results are reflective of the findings and behavioral trends noted for all cases in each mixing class.
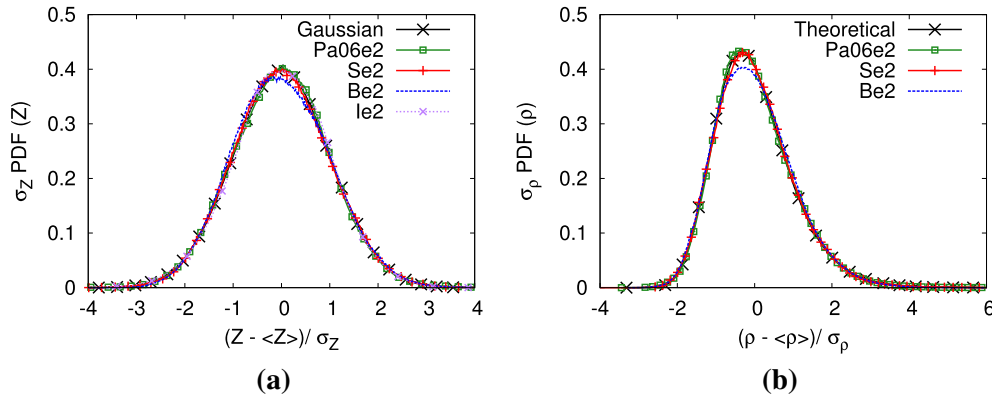
4.3 The density field

It is generally accepted that a scalar field subject to isotropic incompressible turbulent conditions has a nearly Gaussian probability density function (PDF) [7,14,16,17]. To verify that this is preserved when density is nonconstant, focus is placed on four representative test cases (Table 4). The PDFs of the scalar fields in cases Se2 (non-buoyant), Be2 (buoyant), Pa06e2 (partially buoyant), and Ie2 (constant density) are calculated. As shown in Fig. 1a, the scalar fields in all cases are approximately Gaussian.

Table 3 Partially buoyantly driven turbulent flows under the proposed configuration with $Sc = 1$ and $A = 0.13$

No.	α	ϵ	Q	Re	$|g|$	Ri	$\kappa_{max}\eta$	N^3
Pa0006e02	0.006	0.196	0.112	164	0.20	0.09	1.36	96^3
Pa003e002	0.028	0.018	9.85×10^{-3}	70	0.10	0.08	1.64	64^3
Pa003e01	0.031	0.144	0.079	153	0.40	0.11	1.47	96^3
Pa01e01	0.126	0.109	0.053	153	0.60	0.26	1.57	96^3
Pa01e008	0.131	0.080	0.038	144	0.50	0.24	1.70	96^3
Pa02e005	0.246	0.047	0.019	121	0.50	0.39	1.94	96^3
Pa03e009	0.254	0.092	0.038	177	0.75	0.41	1.64	96^3
Pa04e003	0.417	0.032	9.85×10^{-3}	133	0.50	0.58	2.14	96^3
Pa05e04	0.470	0.430	0.122	347	3	0.89	1.49	128^3
Pa05e08	0.500	0.820	0.219	456	5	0.91	1.90	192^3
Pa05e5	0.530	4.68	1.230	672	17	1.00	2.46	384^3
Pa05e008	0.543	0.079	0.019	215	1.00	0.70	1.71	96^3
Pa06e2	0.570	2.00	0.455	711	9	1.05	2.03	256^3
Pa06e4	0.620	4.39	0.898	902	15	0.96	2.50	384^3
Pa06e01	0.640	0.100	0.019	234	1.50	1.08	1.60	96^3
Pa08e4	0.840	4.31	0.301	1011	15	0.91	2.51	384^3
Pa1e01	1.000	0.106	2.41×10^{-6}	309	1.75	1.10	1.60	96^3

Table 4 Four selected representative test cases taken from Tables 1, 2, and 3 ($Sc = 1$, $N^3 = 256^3$)

No.	α	ϵ	Q	Re	$|g|$	Ri	$\kappa_{max}\eta$	A
Se2	0	2.01	1.07	326	0	0	2.02	0.13
Ie2	0	2.01	1.07	417	0	0	2.02	0
Pa06e2	0.57	2.00	0.455	711	9	1.05	2.03	0.13
Be2	1	2.22	0	957	12	1.10	1.99	0.13

Fig. 1 Probability density functions of the scalar, Z, and density, ρ, fields for cases in Table 4. **a** Scalar field distribution. **b** Density field distribution

Additionally, the PDFs of the density fields for cases Se2, Be2, and Pa06e2 are calculated, and they are depicted in Fig. 1b. As the scalar field is Gaussian in distribution and the density field is defined in terms of the scalar field (Eq. 5), a theoretical distribution for the density field can be expressed analytically as,

$$\text{PDF}(\rho) = \frac{1}{a\rho^2\beta\sqrt{2\pi}} \exp\left(-\frac{1}{2\beta^2}\left\{\frac{1}{a}\left(\frac{1}{\rho} - b\right) - \langle Z\rangle\right\}^2\right), \tag{37}$$

which produces the curve denoted "Theoretical" in Fig. 1b. Note the close agreement between this theoretical PDF curve and the PDF data calculated from the density field data. Consistent with previous studies of variable density turbulent mixing [3–5], the density PDFs in all test cases are skewed toward lower density values.

Table 5 Mean ($\langle X \rangle$), variance (σ_X^2), skewness (S_X), and flatness (F_X) of the scalar (Z) and density (ρ) fields obtained in cases Se2, Be2, Pa06e2, and Ie2

No.	$\langle Z \rangle$	σ_Z^2	S_Z	F_Z	$\langle \rho \rangle$	σ_ρ^2	S_ρ	F_ρ
Se2	0.091	0.93	0.052	2.99	1.00	0.015	0.705	4.14
Ie2	0.000	1.00	−0.118	3.17	1.00	0	–	–
Pa06e2	0.092	0.92	0.044	3.12	1.00	0.015	0.746	4.24
Be2	0.095	0.95	0.131	2.88	1.00	0.015	0.557	3.42

To be more quantitative, the skewness (S) and flatness (F) are calculated for cases Se2, Be2, Pa06e2, and Ie2 according to,

$$S_X = \frac{\langle (X - \langle X \rangle)^3 \rangle}{\langle (X - \langle X \rangle)^2 \rangle^{3/2}} \quad F_X = \frac{\langle (X - \langle X \rangle)^4 \rangle}{\langle (X - \langle X \rangle)^2 \rangle^2}. \tag{38}$$

The results are listed in Table 5. It is known that a Gaussian (normal) distribution has a skewness value of zero and a flatness (kurtosis) value of three. The data included in Table 5 suggest a nearly Gaussian distribution in the scalar field, while confirming the non-Gaussianity of the density field distribution.

Based on these findings, the current formulation is capable of sustaining variable density mixing consistent with previously published results under any (buoyant or non-buoyant) flow condition. Further, it offers a straightforward way to determine the needed values of a and b in the equation of state to get a desired Atwood number. Using the results of Fig. 1a, which shows that the scalar field is distributed about a mean of zero ($\langle Z \rangle \approx 0$), and using Eq. 37, it can be written as,

$$\langle \rho \rangle \approx 1/b,$$
$$\sigma_\rho \approx \sigma_Z a, \tag{39}$$

and, consequently,

$$A \approx \frac{a}{b}\sigma_Z \approx \frac{a}{b}\beta. \tag{40}$$

In the present work and without loss of generality, the scalar variance is set to unity ($\beta^2 = 1$), and the density field is prescribed to have a mean of unity ($b = 1$). The desired Atwood number is obtained, then, by specifying the value of the coefficient a.

Other statistics of the scalar field were also evaluated to investigate the differences between isotropic turbulence and buoyant turbulence on the scalar field. In summary, as observed for the distribution of mixture fraction, there were no distinguishable differences in the scalar energy spectra. This led to similar mean scalar dissipation rates (Eq. 21) for a given imposed scalar variance. In other words, the scalar integral timescales, defined as $\tau_Z = \sigma_Z^2/\chi$, were similar for both sources of turbulence. A similar behavior was observed for the scalar integral length scales.

4.4 The velocity field

With the density field behaving as desired, the velocity fields generated under the proposed method are now considered. The PDFs of the normal stresses are first calculated (Fig. 2). Under non-buoyant conditions, the three normal stress components are equivalent (i.e., the flow is isotropic), as is to be expected. Then, as the power ratio is increased from $\alpha = 0$ to $\alpha = 1$, the PDFs begin to differentiate (Fig. 2). While the normal stresses from the velocity components orthogonal to gravity (u and w) remain equivalent, the velocity component aligned with gravity (v) behaves differently. This is related to the larger variance ($\sigma_v^2 = \langle v^2 \rangle - \langle v \rangle^2$) found in the v component relative to the u and w components. The non-buoyant data are reflective of isotropic energy production. The buoyant and partially buoyant cases are subject to anisotropic energy production, as turbulent kinetic energy is preferentially supplied to the v component.

The trends observed in the PDFs of the velocity field stress components have implications for other flow parameters, specifically the characteristic length scale defined in Eq. 28. To determine the effect of the power density ratio on the characteristic length scale imposed on the fluid system, all of the simulation data contained in Tables 1, 2, and 3 are considered. Under purely non-buoyant mixing conditions ($\alpha = 0$), it is found that the ratio
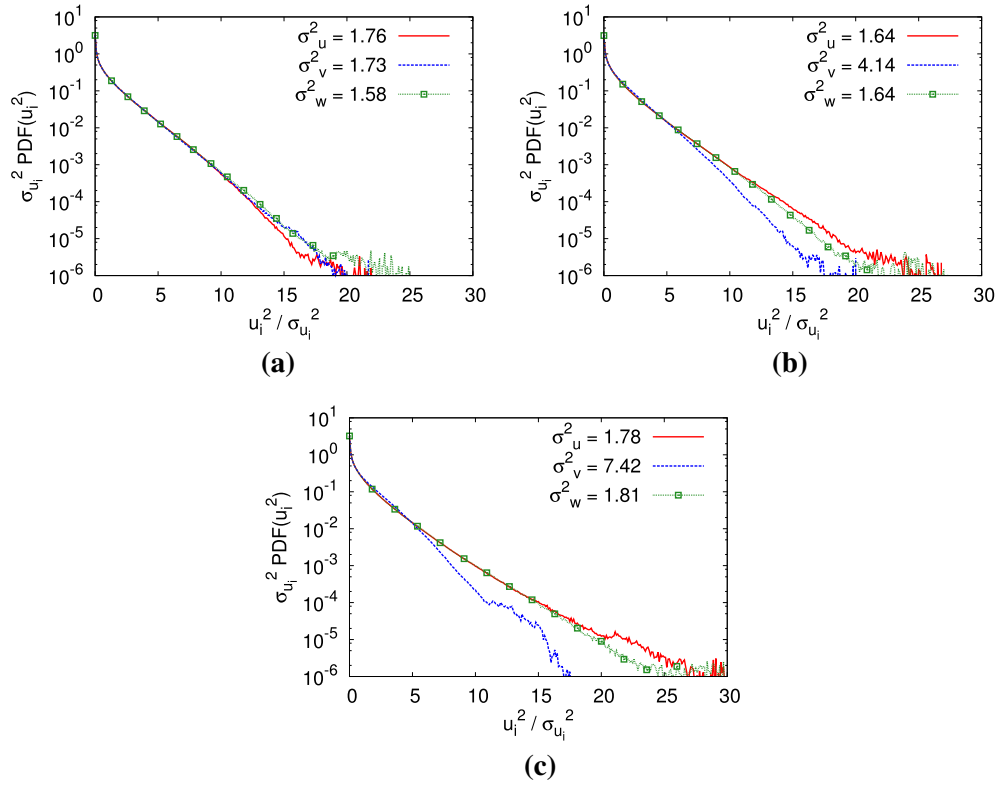
Fig. 2 Probability density functions (PDFs) of the normal stresses for the variable density test cases in Table 4. The variances of each of the velocity components are denoted as σ^2. **a** Non-buoyant (case Se2). **b** Partially buoyant (case Pa06e2). **c** Buoyant (case Be2)

of the integral length scale and the domain size oscillates about $l/L \approx 0.19$ (Fig. 3a). Note that this finding is consistent with results from constant density simulations performed by others [11]. Under purely buoyant mixing conditions ($\alpha = 1$), it is found that $l/L \approx 0.38$ (Fig. 3b). These ratios define the limiting values of l/L under the present simulation method. To determine the integral length scale for partially buoyant cases, the power ratio, α, must be considered. As illustrated in Fig. 3c, as the power ratio tends toward that of a purely buoyant flow ($\alpha \to 1$), the length scale predicted progressively approaches that found in Fig. 3b. Similarly, as the power ratio tends toward that of a purely non-buoyant flow ($\alpha \to 0$), the length scale moves toward the one found in Fig. 3a.

Time-averaged length scales are extracted from each of the simulation results, and their functional dependence on α is depicted in Fig. 3d. There is an approximately linear relationship between the length scale imposed and the power density ratio. As progressively more of the power supplied to the fluid system is provided by buoyant forces, the characteristic length scale grows. This finding is consistent with the trends noted in the PDFs of the normal stresses; the larger magnitude of the v component variance under buoyant (or partially buoyant) conditions results in a larger overall length scale.

The larger v variance also affects the integral timescale. As the total dissipation rate is kept constant when the power ratio is changed, the integral timescale, defined as $\tau_c = l/u_{\mathrm{RMS}} = l^{2/3}\varepsilon^{-1/3}$, increases simultaneously when the integral length scale increases. An increase by a factor of about 1.6 was observed between purely isotropic and purely buoyant turbulent flows. Given the almost constant scalar timescale, τ_Z (Sect. 4.3), the ratio of velocity to scalar timescales was found to vary between 1.35 and 0.86 for the purely isotropic (case Se2) and purely buoyant turbulent flows (case Be2), respectively.

4.5 The buoyant flow field

To investigate how turbulent mixing is affected by the presence of buoyancy effects, it is necessary to understand the buoyant energy production mechanism. Buoyant energy production is dependent on the correlation between the density field and the component of velocity aligned parallel to the gravity vector, as shown in
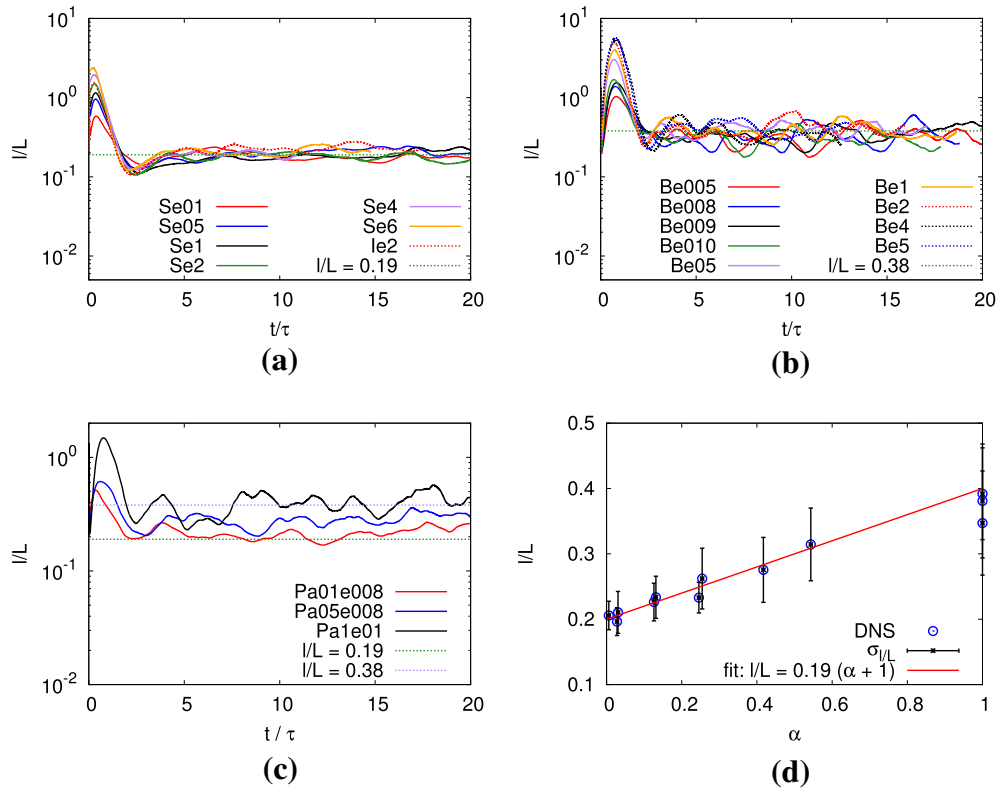
Fig. 3 Characteristic length scale under non-buoyant (Table 1), buoyant (Table 2), and partially buoyant (Table 3) conditions. In (**d**), DNS data are included as *open circles*, and an approximate linear fit is shown. The standard deviation is determined according to: $\sigma_{l/L} = \sqrt{\langle (l(\alpha, t)/L)^2 \rangle - \langle l(\alpha, t)/L \rangle^2}$. **a** Non-buoyant ($\alpha = 0$): $l/L \approx 0.19$. **b** Buoyant ($\alpha = 1$): $l/L \approx 0.38$. **c** Partially buoyant. **d** Relationship between α and l/L
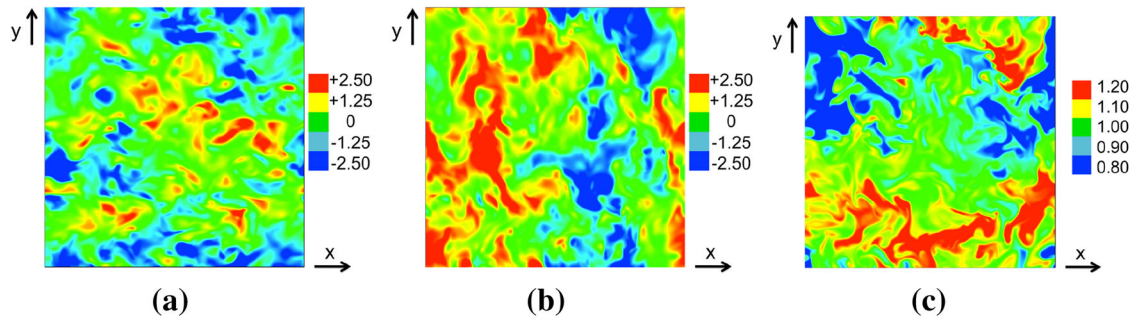
Fig. 4 Contour plots of field variables from case Se2. **a** u component of velocity. **b** v component of velocity. **c** ρ field

Eq. 16 ($\langle \rho' v \rangle g / \langle \rho \rangle$). As the strength of buoyant effects can be quantified through the power density ratio, the dependence of $\langle \rho' v \rangle g / \langle \rho \rangle$ on α needs to be characterized. This dependence can be determined by revisiting the density field (Sect. 4.3) and the velocity field (Sect. 4.4).

4.5.1 Contour plots

Qualitatively, the dependence of the velocity field on the density field can be observed through examination of contour plots. Two-dimensional planar cuts of the u, v, and ρ fields are provided in Figs. 4 and 5 for cases Se2 and Be2, respectively. These represent cuts at the midplane in z direction. Recall that g is in the y direction. The w velocity component is not included here, as it is statistically equivalent to the u component.
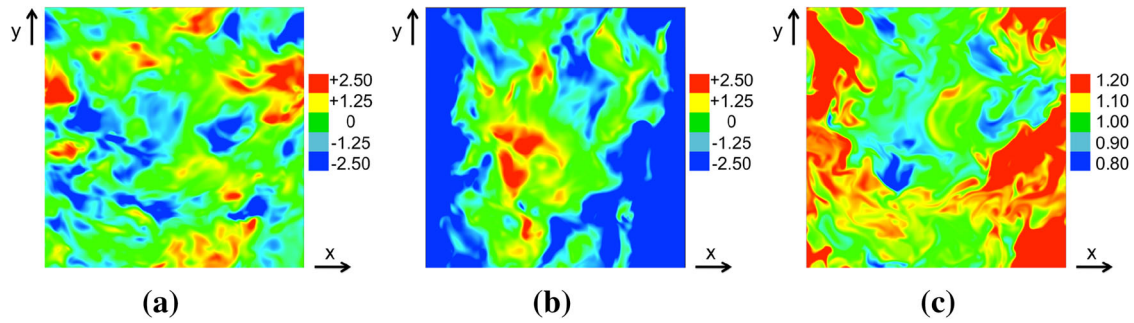
Fig. 5 Contour plots of field variables from case Be2. **a** u component of velocity. **b** v component of velocity. **c** ρ field
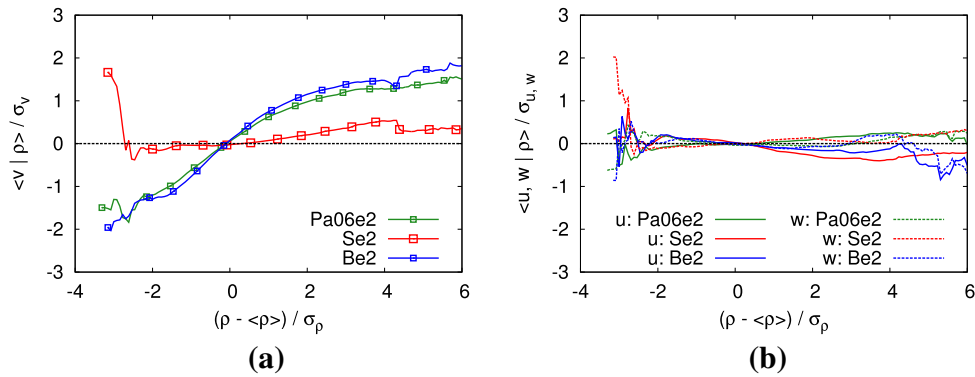
Fig. 6 Conditional averages of the velocity components on the density for the cases in Table 4. **a** Component parallel to gravity. **b** Components perpendicular to gravity

Figure 4 suggests that there is no correlation between the velocity field and the density field. As the non-buoyant case implements an isotropic forcing term, it is expected that the velocity field components would not display any directional dependence. However, consistent with its energy production term, Fig. 5 depicts a clear correlation between the v velocity component and the density field, while the u component field exhibits no such correlation. In regions of low density in Fig. 5c, there are corresponding regions of upward moving fluid in Fig. 5b; in the regions of high density in Fig. 5c, there are corresponding regions of downward moving fluid in Fig. 5b.

4.5.2 Conditional averages

The physical traits illustrated in Figs. 4 and 5 can be more quantitatively expressed by considering the conditional averages of the velocity field components (u, v, and w) on the density field. A vanishing conditional average indicates that the two flow parameters are decorrelated from each other; a nonzero conditional average indicates a correlation between flow variables. The conditional average of the three velocity components on the density field is shown in Fig. 6.

Figure 6a suggests a correlation between the v velocity field and the ρ field, and this correlation becomes stronger as the power density ratio increases from $\alpha = 0$ to $\alpha = 1$. This behavior is both consistent with the contour plots presented, and it is reasonable, as a heavy fluid ($\rho > \langle\rho\rangle$) will fall ($v < 0$) and a light fluid ($\rho < \langle\rho\rangle$) will rise ($v > 0$). Further, Fig. 6c confirms the negligible correlation between the u and w components and the ρ field, as depicted in Figs. 4 and 5. As a note, the large conditional average values present at small density values ($\rho - \langle\rho\rangle < 2\sigma_\rho$) are not statistically meaningful, as they are infrequent occurrences contained in the tails of the density field PDFs (Fig. 1b).

4.5.3 Importance of the power density ratio

In Sect. 4.3, it was shown that a statistically stationary variance can be maintained in the density field under any flow condition (non-buoyant, partially buoyant, or buoyant). Sections 4.4, 4.5.1, and 4.5.2 showed that
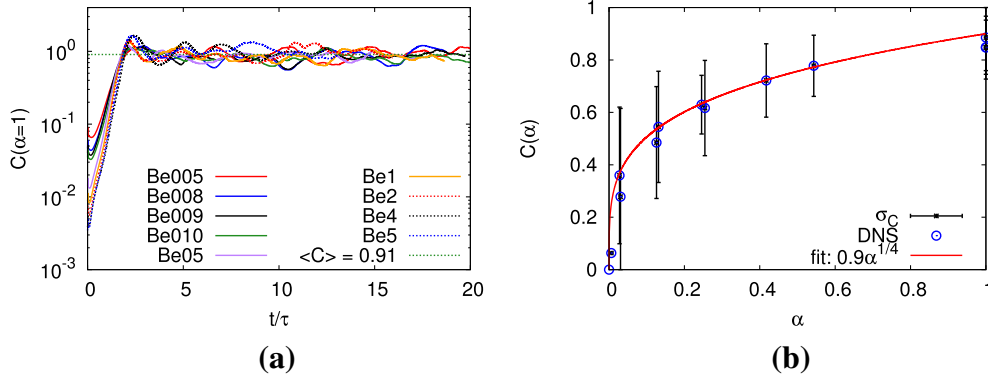
Fig. 7 Effect of power ratio (α) on the constant of proportionality [$C(\alpha)$]. DNS data are included as *open circles*, and an approximate curve fit is shown. The standard deviation is determined according to: $\sigma_{C(\alpha)} = \sqrt{\langle C(\alpha, t)^2 \rangle - \langle C(\alpha, t) \rangle^2}$. **a** $C(\alpha = 1)$ for purely buoyant conditions. **b** Dependence of $C(\alpha)$ on α
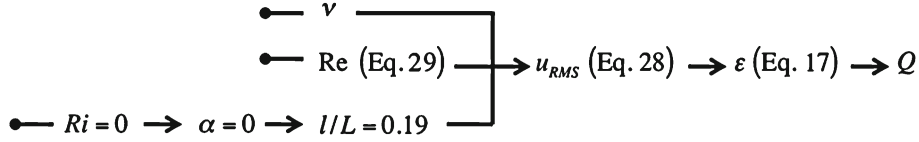
Fig. 8 Flow chart describing non-buoyant simulations ($\alpha = 0$, $g = 0$)

a constant variance could be sustained in the velocity field and that its correlation with the density field is a function of the power density ratio. These flow features are now connected to define the effect of α on buoyant energy production.

Using Bayesian statistics, it can be written,

$$\langle \rho v \rangle (\alpha) = \int \rho \langle v | \rho \rangle (\alpha) \, \text{PDF}(\rho) \, d\rho, \tag{41}$$

which provides the means by which the density field and velocity field effects can be connected. Note that the density field distribution is independent of the power density ratio (Fig. 1b), but the conditional average term is dependent on the power density ratio (Fig. 6a). The result is that the correlation term is a function of α also. To characterize the behavior of the buoyant production term as a function of power density ratio, a scaling approach is instructive. The buoyant production term can be expressed as,

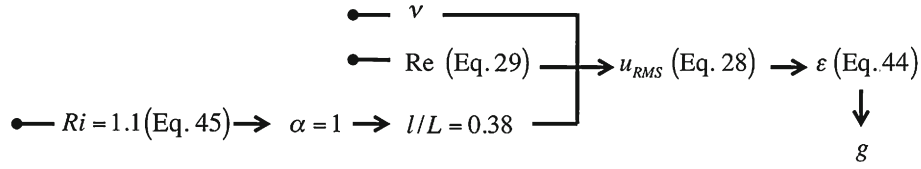$$\langle \rho' v \rangle = C(\alpha) \, \sigma_\rho u_{\text{RMS}}, \tag{42}$$

where $C(\alpha)$ is unitless and of order one.

The purely buoyant flow condition is first examined, as this can be used to define the (upper) limiting behavior of $C(\alpha)$. The test cases listed in Table 2 are examined, and it is found that for all test cases, there is convergence of $C(\alpha = 1)$ toward a value of approximately 0.91 (Fig. 7a). As with the buoyant data, the partially buoyant data (see Table 3) are examined. It is found that a unique value for C is emerged for each power density ratio (Fig. 7b). Within the indicated standard deviation bounds, the data can be adequately captured by a power law ($C(\alpha) = 0.9\alpha^{1/4}$). As to be expected, $C(\alpha)$ increases monotonically as the power density ratio increases.

5 Using the developed simulation framework

The procedure needed to perform (and control) non-buoyant, buoyant, and partially buoyant mixing simulations is now outlined. The success of this simulation method hinges on the ability to control the relative magnitude of buoyant and non-buoyant body forces acting on the mixing fluids. By manipulating the relative magnitude of these two summed terms through the power density ratio (α), the full range of purely buoyant and purely non-buoyant cases can be simulated.

$$\nu \quad \mathrm{Re}\,(\mathrm{Eq.}\,29) \longrightarrow u_{RMS}\,(\mathrm{Eq.}\,28) \longrightarrow \varepsilon\,(\mathrm{Eq.}\,44)$$

$$Ri = 1.1\,(\mathrm{Eq.}\,45) \longrightarrow \alpha = 1 \longrightarrow l/L = 0.38 \qquad \downarrow$$

$$g$$

Fig. 9 Flow chart describing buoyant simulations ($\alpha = 1$, $Q = 0$)

5.1 Non-buoyant simulations

The flow chart depicted in Fig. 8 illustrates the process needed to simulate purely non-buoyant mixing. Once it is decided that the simulation is to be purely non-buoyant, the characteristic length scale is known (Fig. 3a, $l/L = 0.19$). This leaves two degrees of freedom to be selected. The first is the kinematic viscosity, ν, and the second is the Reynolds number to be achieved. The maximum possible Reynolds number achieved can be expressed in terms of the number of grid points in one direction, N, and the grid resolution ($\kappa_{\max}\eta = (N/2)(\nu^3/\epsilon)^{1/4}$),

$$Re_{\max} = \left(\frac{2}{N}\frac{1}{l}\kappa_{\max}\eta\right)^{-4/3}. \tag{43}$$

Once the grid size (N) and the desired resolution ($\kappa_{\max}\eta \geq 1.5$, in general [36]), are chosen, the Reynolds number is defined. Then, using the Reynolds number, the length scale, and the viscosity, the root-mean-square velocity, u_{RMS}, may be evaluated. From these, the total energy dissipation rate can be calculated. As this is a non-buoyant simulation, it can be written that $\epsilon = 2Q$ (assuming the two dilatation terms in Eq. 17 are negligible), from which the needed forcing coefficient, Q, is determined. The desired Schmidt number can then be used to select the diffusion coefficient: $\mathcal{D} = \nu/Sc$. Lastly, the Atwood number can be controlled by varying the a and b values, as discussed in Sect. 4.3.

5.2 Buoyant simulations

A similar process is used for purely buoyant simulations, and this process is illustrated in Fig. 9. Following Fig. 3b, purely buoyant flows impose a characteristic length scale of $l/L = 0.38$. Following the choice of kinematic viscosity (ν) and selecting the grid size (N) needed for the desired Reynolds number ($Re_{\max}$), the root-mean-square velocity can be calculated. These, in turn, define the total energy dissipation rate, ϵ. Following Fig. 7a, the needed value of g for any purely buoyant simulation can be determined according to,

$$g = \frac{\epsilon}{C(\alpha = 1)Au_{RMS}} = \frac{\epsilon}{0.91Au_{RMS}}. \tag{44}$$

Once again, the two dilatation terms in Eq. 17 were assumed to be negligible. Similar to the non-buoyant case, the Schmidt and Atwood numbers can then be fixed via the choice of $\mathcal{D}$, a, and b.

It should be noted that there is only one Richardson number possible for an $\alpha = 1$ condition. Using the definition of Ri (Eq. 30), the definition of l (Eq. 28), and the global energy balance for buoyant flows (Eq. 44), it can be obtained,

$$Ri = \frac{1}{C(\alpha = 1)} = 1.1. \tag{45}$$

5.3 Partially buoyant simulations

The procedure to simulate partially buoyant simulations is now discussed (Fig. 10). Initially, the process is similar to the other two. There are three free parameters available, the kinematic viscosity (ν), the grid size (N), and the power density ratio (α). Once the power density ratio is specified, the length scale ratio (l/L) is known (Fig. 3d). Then, the Reynolds number is determined by the resolution desired and the grid size (Eq. 43). Using these three values, the root-mean-square velocity and the total energy dissipation rate can be calculated.
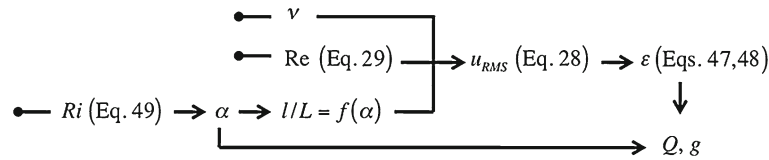
Fig. 10 Flow chart describing partially buoyant simulations

Similar to the buoyant case, the global energy balance for ϵ can be used to determine the Q and g values needed for a given partially buoyant condition. Assuming the two dilatation terms in Eq. 17 are negligible, the stationary global energy balance can be written,

$$\epsilon = 2Q + C(\alpha) \, A \, g \, u_{\text{RMS}}. \tag{46}$$

When used in concert with the definition of Ri (Eq. 30), the integral length scale (Eq. 28), and the power density ratio (Eq. 18), it is found,

$$g = \frac{\epsilon \, \alpha}{C(\alpha) \, A \, u_{\text{RMS}}}, \tag{47}$$

$$Q = \frac{\epsilon \, (1 - \alpha)}{2}, \tag{48}$$

$$Ri = \frac{\alpha}{C(\alpha)}. \tag{49}$$

Using the above equation, the Ri can be evaluated from the power density ratio. Alternatively, the power density ratio can be obtained from the Ri. Following this, the Schmidt and Atwood numbers can be specified.

6 Summary and conclusions

In this work, we proposed a new mathematical framework for the numerical simulation of turbulent buoyant flows. In contrast to previous high-fidelity direct numerical simulations of traditional Rayleigh–Taylor instabilities primarily focused on the large-scale behavior [1,2], the focus was placed on developing a computationally efficient framework to investigate the small-scale dynamics of turbulent buoyant flows.

The geometry adopted was the same as that of Batchelor et al. [8], Livescu et al. [3,4,6], and Soulard et al. [24], namely a triply periodic domain of homogeneous turbulence. This geometry was preferred over the original Rayleigh–Taylor configuration [1,2], as it reduces the computational cost of performing the simulations. Unfortunately, without the presence of the two reservoirs of heavy and light densities of the traditional RT configuration, the resulting homogeneous turbulent flow is unsteady [6,8]. Initially, the turbulent kinetic energy increases due to production by buoyant forces. Then, after homogenization of the density field, the turbulent kinetic energy decreases due to dissipation by viscous forces.

As an alternative to this unsteady configuration, we proposed to sustain the turbulent flow field at a state of constant turbulent kinetic energy by supplementing the mixture fraction equation with a source term in a manner similar to the work of Soulard et al. [24]. They used the scalar mean gradient forcing technique [14,15] in the direction of gravity to generate a statistically stationary homogeneous turbulent flow. Unfortunately, the scalar mean gradient is known to create anisotropy in the scalar field [26] that is difficult to distinguish from the anisotropy generated by gravity.

In order to separate the effects of buoyancy from those due to large-scale gradients (present in Soulard's work and in the traditional RT configuration), we proposed to replace the mean scalar gradient with the recently developed linear scalar forcing [26]. This forcing technique has the advantage of preserving the inherent nature of the density field without introducing any artificial anisotropy. In addition, we supplemented the momentum equation with an additional source term to provide pseudo-shear energy production [10,11,25]. With these modifications, the present framework can simulate any homogeneous turbulent flows from purely isotropic turbulence (HIT) to purely buoyant turbulence (HBT). Four nondimensional parameters can be adjusted independently, namely the Reynolds number, Re, the Richardson number, Ri, the Atwood number, A, and the Schmidt number, Sc.

Test cases spanning a range of Reynolds and Richardson numbers have been presented and examined. First, it was observed that neither the variable density nature nor the buoyant nature of the turbulent flow field

influences the mixture fraction field; its distribution remains very close to a Gaussian, which is characteristic of passive scalar mixing. On the other hand, anisotropy starts to develop in the velocity field as the Richardson number is increased; the variance of the velocity component in the direction of gravity increases. Simultaneously, a conditional dependence is introduced in this velocity component with respect to the local density: Heavier (resp. lighter) fluid tends to move in the direction of gravity (resp. in the opposite direction). While this result may not be surprising for laminar or turbulent Rayleigh–Taylor configurations, it is interesting to note that these concerted fluctuations are still present in homogeneous flows and contribute to most of the variance in the velocity component (more than 75 %). Finally, these concerted fluctuations are the mechanism by which energy is produced in buoyant flows.

These results highlight critical differences between isotropic and buoyant homogeneous turbulent flows and suggest directions to investigate for future subgrid-scale modeling for applications in large-eddy simulations.

References

1. Cook, A.W., Cabot, W., Miller, P.L.: The mixing transition in Rayleigh–Taylor instability. J. Fluid Mech. **511**, 333–362 (2004)
2. Cabot, W.H., Cook, A.W: Reynolds number effects on Rayleigh–Taylor instability with possible implications for type Ia supernovae. Nat. Phys. **2**, 562–568 (2006)
3. Livescu, D., Ristorcelli, J.R.: Variable-density mixing in buoyancy-driven turbulence. J. Fluid Mech. **605**, 145–180 (2008)
4. Livescu, D., Ristorcelli, J.R., Gore, R.A., Dean, SH., Cabot, W.H., Cook, A.W.: High-Reynolds number Rayleigh–Taylor turbulence. J. Turbul. **10**, N13 (2009)
5. Livescu, D., Ristorcelli, J.R., Petersen, M.R., Gore, R.A.: New phenomena in variable-density Rayleigh–Taylor turbulence. Phys. Scr. **T142**, 014015 (2010)
6. Livescu, D., Ristorcelli, J.R.: Buoyancy-driven variable-density turbulence. J. Fluid Mech. **591**, 43–71 (2007)
7. Chung, D., Pullin, D.I.: Direct numerical simulation and large-eddy simulation of stationary buoyancy-driven turbulence. J. Fluid Mech. **643**, 279–308 (2010)
8. Batchelor, G.K., Canuto, V.M., Chasnov, J.R.: Homogeneous buoyancy-generated turbulence. J. Fluid Mech. **235**, 349–378 (1992)
9. Alvelius, K.: Random forcing of three-dimensional homogeneous turbulence. Phys. Fluids **11**, 1880–1889 (1999)
10. Lundgren, T.S.: Linearly-forced isotropic turbulence. Annu. Res. Briefs Cent. Turbul. Res. **2**, 461–473 (2003)
11. Rosales, C., Meneveau, C.: Linear forcing in numerical simulations of isotropic turbulence: physical space implementations and convergence properties. Phys. Fluids **17**, 095106 (2005)
12. Eswaran, V., Pope, S.B.: An examination of forcing in direct numerical simulations of turbulence. Comput. Fluids **16**, 257–278 (1988)
13. Eswaran, V., Pope, S.B.: Direct numerical simulations of the turbulent mixing of a passive scalar. Phys. Fluids **31**, 506–520 (1988)
14. Yeung, P.K.: Lagrangian characteristics of turbulence and scalar transport in direct numerical simulations. J. Fluid Mech. **427**, 241–274 (2001)
15. Donzis, D.A., Sreenivasan, K.R., Yeung, P.K.: The Batchelor spectrum for mixing of passive scalars in isotropic turbulence. Flow Turbul. Combust. **85**, 549–566 (2010)
16. Watanabe, T., Gotoh, T.: Statistics of a passive scalar in homogeneous turbulence. New J. Phys. **6**, 40 (2004)
17. Gotoh, T., Hatanaka, S., Miura, H.: Spectral compact difference hybrid computation of passive scalar in isotropic turbulence. J. Comput. Phys. **231**, 7398–7414 (2012)
18. Livescu, D.: Numerical simulations of two-fluid turbulent mixing at large density ratios and applications to the Rayleigh–Taylor instability. Philos. Trans. R. Soc. A **371**, 20120185 (2013)
19. Majda, A.: Compressible fluid flow and systems of conservation laws in several space variables. Appl. Math. Sci. **53**, pp. 72–79 (1984)
20. Majda, A., Sethian, J.A.: Derivation and numerical solution of the equations of low Mach number combustion. Combust. Sci. Technol. **42**, 185–205 (1985)
21. Desjardins, O., Blanquart, G., Balarac, G., Pitsch, H.: High order conservative finite difference scheme for variable density low Mach number turbulent flows. J. Comput. Phys. **227**, 7125–7159 (2008)
22. Haworth, D.C.: Progress in probability density function methods for turbulent reacting flows. Prog. Energy Combust. Sci. **36**, 168–259 (2010)
23. Almgren, A., Bell, J., Nonaka, A., Zingale, M.: Low Mach number modeling of stratified flows. In: Finite Volumes for Complex Applications VII—Methods and Theoretical Aspects, Springer Proceedings in Mathematics & Statistics, vol. 77. Springer, Berlin (2014)
24. Soulard, O., Griffond, J., Grea, B.-J.: Large-scale analysis of self-similar unstably stratified homogeneous turbulence. Phys. Fluids **26**, 015110 (2014)
25. Carroll, P.L., Blanquart, G.: A proposed modification to Lundgren's physical space velocity forcing method for isotropic turbulence. Phys. Fluids **25**, 105114 (2013)

26. Carroll, P.L., Verma, S., Blanquart, G.: A novel forcing technique to simulate turbulent mixing in a decaying scalar field. Phys. Fluids **25**, 095102 (2013)
27. Mydlarski, L., Warhaft, Z.: On the onset of high-Reynolds-number grid-generated wind tunnel turbulence. J. Fluid Mech. **320**, 331–368 (1996)
28. Carroll, P.L., Blanquart, G.: The effect of velocity field forcing techniques on the Karman–Howarth equation. J. Turbul. **15**, 429–448 (2014)
29. Vallis, G.K.: Atmospheric and Oceanic Fluid Dynamics: Fundamentals and Large-Scale Circulation. Cambridge University Press, New York (2006)
30. Morinishi, Y., Vasilyev, O.V., Ogi, T.: Fully conservative finite difference scheme in cylindrical coordinates for incompressible flow simulations. J. Comput. Phys. **197**, 686–710 (2004)
31. Harlow, F.H., Welch, J.E.: Numerical calculation of time-dependent viscous incompressible flow of fluid with free surface. Phys. Fluids **8**, 2182–2189 (1965)
32. Kim, J., Moin, P.: Application of a fractional-step method to incompressible Navier–Stokes equations. J. Comput. Phys. **59**, 308–323 (1985)
33. Pierce, C.D., Moin, P.: Progress-variable approach for large eddy simulation of turbulent combustion. Ph.D. thesis. Rep. TF80, Flow Physics and Computation Division, Dept. Mech. Eng. Stanford Univ. (2001)
34. Savard, B., Xuan, Y., Bobbitt, B., Blanquart, G.: A computationally-efficient, semi-implicit, iterative method for the time-integration of reacting flows with stiff chemistry. J. Comput. Phys. (2015). doi:10.1016/j.jcp.2015.04.018
35. Nourgaliev, R.R., Theofanous, T.G.: High-fidelity interface tracking in compressible flows: unlimited anchored adaptive level set. J. Comput. Phys. **224**, 836–866 (2007)
36. Pope, S.B.: Turbulent Flows. Cambridge University Press, Cambridge (2000)